Interference of excitons and surface plasmons in the optical absorption spectra of monolayer and bilayer graphene

Hsiang-Lin Liu, Bergitta Dwi Annawati, Nguyen Tuan Hung, Desman Perdamaian Gulo, Pablo Solís-Fernández, Kenji Kawahara, Hiroki Ago, and Riichiro Saito

Phys. Rev. B **107**, 165421 — Published 26 April 2023

DOI: 10.1103/PhysRevB.107.165421

Interference of exciton and surface plasmon in the optical absorption spectra of monolayer and bilayer graphene

Hsiang-Lin Liu[1,*], Bergitta Dwi Annawati[1], Nguyen Tuan Hung[2,3], Desman Perdamaian Gulo[1], Pablo Solís-Fernández[4], Kenji Kawahara[4], Hiroki Ago[4], and Riichiro Saito[2]

[1]Department of Physics, National Taiwan Normal University, Taipei 11677, Taiwan

[2]Department of Physics, Tohoku University, Sendai 980-8578, Japan

[3]Frontier Research Institute for Interdisciplinary Sciences, Tohoku University, Sendai 980-8578, Japan

[4]Global Innovation Center, Kyushu University, Fukuoka 816-8580, Japan

*Corresponding author: E-mail: hliu@ntnu.edu.tw

Abstract

By using spectroscopy ellipsometry, we investigated the optical absorption spectra of monolayer and bilayer graphene in the deep ultraviolet (UV) region up to 6.42 eV as a function of temperature. The optical absorption spectra of monolayer and bilayer graphene can be fitted by two Breit–Wigner–Fano (BWF) spectral functions, in which each BWF is originated by the interference of discrete excitonic spectra and continuous surface plasmon spectra. Each BWF peak shows narrower linewidth and larger peak intensity with increasing temperature. The unusual temperature dependence of the BWF peaks is understood by a shorter lifetime of the surface plasmon at a higher temperature, which gives a smaller BWF asymmetric parameter. The optical absorption by surface plasmon is usually observed only at the surface of the three-dimensional crystal or two-dimensional material. The contribution of surface plasmon becomes relatively larger in the case of monolayer or bilayer graphene than that of single-crystal graphite because of the two-dimensional nature of electrons. The observed optical absorption spectra are confirmed by calculating the complex dielectric function using the first-principles calculations.

PACS number: 68.65.Pq, 71.35.−y, 73.20.Mf, 78.20.Ci

1. Introduction

In two-dimensional (2D) materials, optical absorption occurs not only through single-particle excitation that includes excitonic excitation but also through collective excitation of electrons, a phenomenon known as surface plasmon polariton [1-5]. Because the bulk plasmon in three-dimensional materials exhibits a longitudinal wave, the bulk plasmon is not excited by a transverse wave of a photon. However, a plasmon at the surface of materials can be excited by light and propagates in the direction parallel to the surface which is known as a surface plasmon. A surface plasmon resonance is commonly used to observe nanoparticles on the metal surface, when the resonance condition for surface plasmon is satisfied [6]. However, evaluating contributions of a surface plasmon and single-particle excitation in the optical absorption spectra are not well-established because the surface plasmon frequency exists not in the visible (or infrared) light region but in the deep UV or terahertz (THz) region, which corresponds to interband or intraband plasmons, respectively [6]. In our previous study, we observed the interference phenomena in the optical absorption of single-crystal graphite in the deep UV region at 4–6 eV [7]. However, we did not discuss the contribution of a surface plasmon in the optical absorption of single-crystal graphite because we could not calculate the optical response at the surface of graphite by the first-principles calculation. Since the surface plasmon phenomenon occurs less than 10 nm away from the surface, the contribution of a surface plasmon to optical absorption is expected to be relatively large in 2D materials. Furthermore, we can calculate the optical response of 2D materials, which includes the effect of surface plasmon by the first-principles calculations. In this work, we investigated the optical absorption up to 6.42 eV for monolayer and bilayer graphene by spectroscopic ellipsometry. We found that the optical absorption peaks become larger and narrower with increasing temperature from 4.5 to 500 K. This unusual behavior is discussed by the temperature-dependent interference effect combined with the first-principles calculations of the complex dielectric function.

Monolayer graphene has attracted considerable attention from condensed matter physicists, chemists, semiconductor device engineers, and material scientists since 2004 [8-11]. Graphene exhibits unusual many-body physics behavior, including strong electron-electron interactions [12] as well as quantum phase transitions and novel

admixtures of these states because of 2D confinement of electrons [13]. Furthermore, graphene has several practical applications, such as in nanoelectronics, optoelectronics, photonics, and information processing, in which surface plasmon has an important role.[14-18]. Bilayer graphene has been recognized as a new material independent of monolayer graphene since 2018. The electronic properties of twisted bilayer graphene are strongly affected by the twist angle, indicating that the electronic band structure is modulated by angle-dependent interlayer interaction. These tunable electronic bands are exceptional because they can host various correlated electronic phases [19-22]. Thus, bilayer graphene has opened new avenues for developing high-performance twistronic devices [23,24].

A systematic study of the optical properties of monolayer and bilayer graphene is essential to fabricate optoelectronics, photonics, and twistronic devices for practical applications. Having knowledge of the temperature-dependent optical properties of a device is crucial to investigate the effect of self-heating on device performance. Furthermore, understanding the frequency-dependent optical properties is essential for improving the quality of materials and the efficiency and applicability of devices. Previous studies have reported that monolayer graphene exhibits intraband Drude conductivity in the THz to far-infrared frequency range and interband universal conductivity in the mid- and near-infrared frequency range. [25-28]. Although many similar observations have been reported thus far, conflicting results have been obtained. Zou *et al.* [29] analyzed the temperature-dependent THz conductivity of bilayer graphene on the quartz substrate. They observed a strong peak at 2.7 THz, which was attributed to the enhancement of the density of states caused by the twisting of the bilayer graphene. Yang *et al.* [30] presented the first-principles calculations of many-body effects on the optical response of monolayer and bilayer graphene. They determined that infrared absorbance per graphene layer becomes approximately constant, whereas the exciton peak appears at 4.5 eV in monolayer and bilayer graphene. Kravets *et al.* [31] examined the spectroscopic ellipsometric spectra of monolayer graphene on the quartz substrate at room temperature. They observed a pronounced asymmetric peak at 4.6 eV, which was associated with a van Hove singularity in the density of states and excitonic effects of graphene. Wurstbauer *et al.* [32] employed image ellipsometry in the visible frequency

range and determined that the optical constants of monolayer graphene were dependent on the SiO_2 and GaAs substrates. Chae *et al.* [33] reported the absorbance spectra of free-standing monolayer and bilayer graphene at room temperature. They observed an asymmetric absorption peak at 4.7 eV, which was attributed to an excitonic resonance. Santoso *et al.* [34] presented the optical conductivity spectra of monolayer and bilayer graphene on SiC substrates at room temperature. They noted that monolayer and bilayer graphene exhibited marked excitation at 5.4 eV, which was a mixture of interband transitions from π to $\pi*$ at the M point and a π plasmonic excitation, and a resonant exciton at 6.3 eV. Li *et al.* [35] and Fang *et al.* [36] have determined the spectroscopic ellipsometric spectra of monolayer and bilayer graphene on the fused silica and sapphire substrates at room temperature. They determined that monolayer and bilayer graphene exhibited a strong absorption peak at 4.8 eV and an additional weak absorption peak at 6.4 eV. These two absorption peaks were attributed to the resonant excitons at the M and Γ points of the Brillouin zone, respectively. El-Sayed *et al.* [37] investigated the effects of SiO_2, quartz, and glass substrates on the optical constants of monolayer graphene through spectroscopic ellipsometry. They observed that the difference in the optical constants of monolayer graphene on the three substrates did not exceed 5%. Wu *et al.* [38] examined the temperature-dependent optical properties of monolayer and bilayer graphene on Si and SiO_2/Si substrates through spectroscopic ellipsometry. They reported that monolayer and bilayer graphene exhibited marked absorption in the UV region. When the temperature was increased from 300 to 500 K, the refractive index of monolayer graphene on Si substrate gradually increased and its extinction coefficient decreased. In addition, Igarashi *et al.* [39], Yanagi *et al.* [40], and Satco *et al.* [41] have observed intersubband plasmon optical absorption in electrochemically-doped carbon nanotube films. Sasaki *et al.* [42] indicated that the interband plasmon was expressed by azimuthal transverse magnetic mode. Satco *et al.* [43] calculated the optical absorption spectra as a function of (n,m) of carbon nanotube and the Fermi energy to examine the intersubband plasmon excitation.

Most optical studies have conducted measurements at room temperature and narrow frequency ranges. However, the lifetime of a plasmon is shorter than that of an electron photoexcited by single-particle excitation, and the lifetime depends on temperature. In

this study, we examined the temperature-dependent optical properties of monolayer and bilayer graphene at 4.5 to 500 K within the spectral range of 0.73 to 6.42 eV through spectroscopy ellipsometry. The wide temperature and spectral ranges enabled us to characterize the dispersion of the complex refractive index, complex dielectric function, and optical absorption coefficient. Furthermore, we compared our experimental results with the calculated complex dielectric function by using the first-principles calculations. The goal of this study is to uncover anomalous deep UV electronic excitation in monolayer and bilayer graphene and to verify many-body interactions. The findings of this study can serve as a valuable reference for quantitatively investigating the effect of temperature- and frequency-dependent electromagnetic response on the performance of graphene-based optoelectronics, photonics, and twistronic devices.

2. Method

2.1 Experiments

Monolayer and bilayer graphene samples were grown on Cu and Cu-Ni alloy thin films by using the chemical vapor deposition (CVD) method [44-47]. The catalyst films were deposited on c-plane sapphire, and graphene was grown by ambient pressure CVD at 1075 °C and 1085 °C for the monolayer and bilayer graphene, respectively. The CVD time for bilayer graphene was 6 hours to make vernal stacking [47]. After growth, graphene was transferred to a sapphire or SiO_2/Si substrate by etching the catalyst film in an aqueous ammonium persulfate solution while protecting graphene with a polymethylmethacrylate (PMMA) thin film, followed by removal of PMMA with acetone. The monolayer and bilayer graphene samples were verified through atomic force microscopy and Raman spectroscopy [44-47]. Spectroscopic ellipsometer measurements were performed at room temperature in the spectral range of 0.73 to 6.42 eV at the incident angles of 55°, 60°, 65°, 70°, and 75° on an M-2000U ellipsometer from J. A. Woollam Co.

We adopted the stacked layer model, including a sapphire substrate, thin film, and surface roughness as well as an air ambient structure, to fit raw ellipsometric parameters of Ψ and Δ [48]. The fitting parameters of the model are listed in Table 1. Through

spectroscopic ellipsometry, we determined that the thicknesses of monolayer and bilayer graphene are 0.36 ± 0.07 and 0.67 ± 0.13 nm, respectively; these values are similar to those reported in the literature [44-47]. The independently measured ellipsometric spectra at different incident angles and the modeled curves are in good agreement, as presented in Supplementary Fig 1. For temperature-dependent ellipsometry measurements at 4.5 to 500 K, the sample was mounted in a Janis ST-400 continuous-flow liquid helium cryostat. Then, the ultrahigh vacuum was applied at a base pressure of 10^{-8} torr at an incident angle of 70° [48-50].

Table 1. Fitted parameters of the stacked layer model for the ellipsometric spectra of monolayer and bilayer graphene.

Layer	Monolayer	Bilayer
Surface roughness (nm)	0.03 ± 0.01	0.06 ± 0.01
Film thickness (nm)	0.36 ± 0.07	0.67 ± 0.13
Sapphire substrate (mm)	0.5	0.5

2.2 Theoretical model

Electronic energy band structures of monolayer and bilayer graphene were determined using the first-principles with Quantum Espresso [57]. The exchange correlation function was calculated using local-density approximation (LDA) [58] and the C.pz-hgh.UPF pseudopotential [59]. LDA usually underestimates the energy bandgap. However, because both monolayer and bilayer graphene have zero bandgap, as shown in Figs. 5(a) and 5(b), LDA is suitable for obtaining the energy band structures of semi-metals. We adopted a cutoff energy of approximately 80 Ry for plane-wave convergence and a k-points mesh of 12 × 12 × 1 for the self-consistent field. For the non-self-consistent field, we used a larger k-points mesh of 150 × 150 × 1 and 100 × 100 × 1 for monolayer and bilayer graphene, respectively, to obtain the convergence of the dielectric function and joint density of state (JDOS). The real and imaginary parts of the dielectric function, $\varepsilon_1(\omega)$ and $\varepsilon_2(\omega)$, and the JDOS were calculated by using epsilon.x code in Quantum Espresso within independent particle approximation (IPA). Compared with the many-body calculations, such as the Bethe-Salpeter equation, which considers electron-hole

interactions and is a time-consuming calculation, IPA is more suitable for determining the optical properties of materials with photon energy of up to 30 eV; such high photon energy is observed in plasmonic excitation [7]. For bilayer graphene, we applied the rVV10 nonlocal correlation functional [60] for the van der Waals interaction. The optimized lattice structures were 2.432 Å and 2.436 Å for the monolayer and bilayer graphene, respectively; these values are consistent with the experimental value of ~ 2.46 Å [61].

3. Results and discussion

In Fig. 1 (a) and 1(b), we present the temperature-dependent refractive index and extinction coefficient spectra of monolayer and bilayer graphene on sapphire substrates, respectively. Similar qualitative results were obtained for the samples on SiO_2/Si substrates, as depicted in Supplementary Fig 2. These data are essential for understanding the optical response of photonic devices at various temperatures and photon energies. The refractive index of monolayer graphene at room temperature decreased with an increase in photon energy from the near-infrared to the visible frequency range. Two maxima were observed in the deep UV region, corresponding to the anomalous dispersion region [51]. Moreover, the refractive index of bilayer graphene was larger in terms of magnitude than that of monolayer graphene. For both monolayer and bilayer graphene, the refractive index slightly increased with increasing temperature in the near-infrared frequency range. The small increase in the refractive index as a function of temperature can be ascribed to enhanced electron–phonon interactions with increasing temperature, as observed for other semiconductors, such as Si, GaAs, and InP [52]. By contrast, the temperature variation of the refractive index was considerably larger in the deep UV frequency range. In Fig. 1, we plot the extinction coefficient, k of (a) monolayer and (b) bilayer graphene as a function of photon energy at room temperature. The spectra of k exhibited a strong absorption and an additional shoulder in the deep UV frequency range. Notably, the intensity of these two absorption peaks increased with increasing temperature.

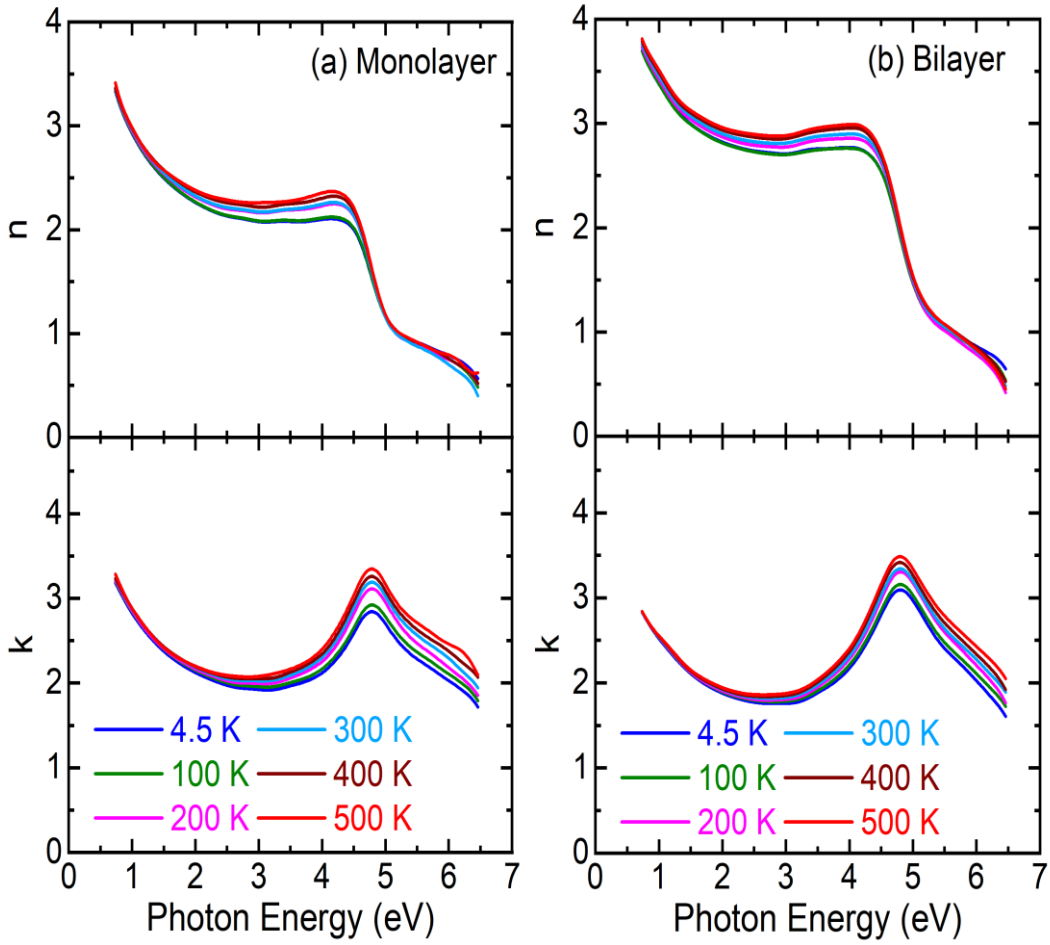

Fig. 1. Temperature-dependent refractive index (up) and extinction coefficient (bottom) spectra of (a) monolayer and (b) bilayer graphene.

Figure 2 depicts the temperature-dependent complex dielectric function of monolayer and bilayer graphene. The dispersion response of the real part ε_1 of the complex dielectric function of monolayer graphene exhibited a positive value up to 4.0 eV at room temperature. This value then decreased to a negative value at approximately 4.89 eV. The photon energy at $\varepsilon_1 = 0$ corresponds to the resonance condition of a plasmon. With an increase in temperature, the zero-point redshifts, which reflects that the plasmon resonance zone became wider and deeper. This tunable optical response is beneficial for graphene-based plasmonic nanodevice applications. In Fig. 2, the optical transitions were identified in the spectra in accordance with resonance and antiresonance features that appeared at the same energy in the real and imaginary parts of the complex dielectric function, respectively. In particular, the imaginary part ε_2 of monolayer and bilayer

graphene was dominated by two optical transitions in the deep UV frequency range. The intensities increased with increasing temperature. The bilayer graphene had an overall larger magnitude in the real and imaginary parts of the complex dielectric function than did monolayer graphene.

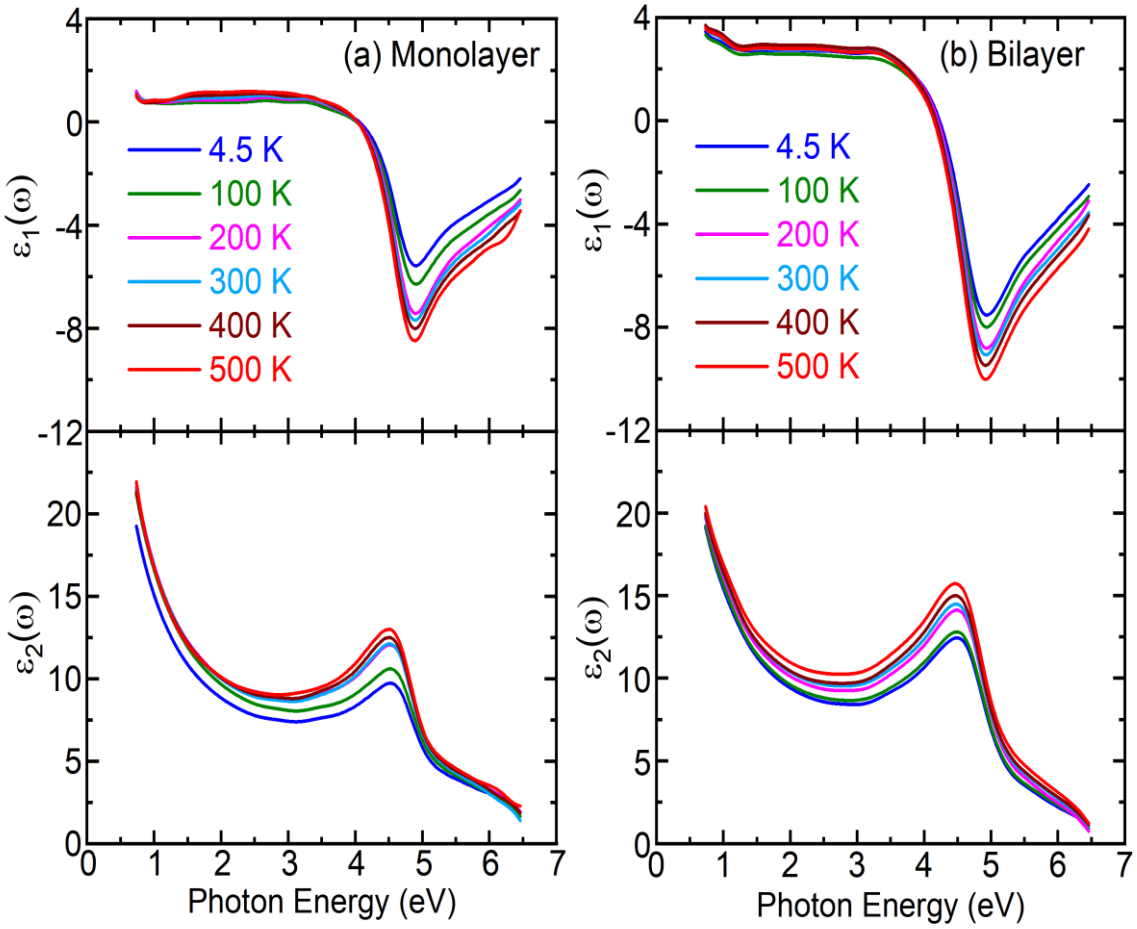

Fig. 2. Temperature-dependent complex dielectric function of (a) monolayer and (b) bilayer graphene.

Figure 3 illustrates the optical absorption coefficient of (a) monolayer and (b) bilayer graphene as a function of photon energy at various temperatures. We calculated α by using complex dielectric function as follows

$$\alpha = \frac{2\omega}{c}\sqrt{\frac{1}{2}\sqrt{\varepsilon_1^2(\omega)+\varepsilon_2^2(\omega)}-\varepsilon_1(\omega)}, \quad (1)$$

where c is the speed of light in vacuum [62]. In Supplementary Fig 3, we compared the α values of monolayer and bilayer graphene with that of single-crystal graphite at 4.5 K [7].

These spectra had three crucial features. First, the α values of monolayer and bilayer graphene at room temperature gradually increased from the near-infrared to the visible frequency range. Both monolayer and bilayer graphene exhibited the maximum α value in the deep UV frequency region. The observed high optical absorption coefficient in the order of 10^6 cm^{-1} is desirable for efficient optical absorbers, such as photodetectors and photocatalysts. Second, the optical absorption coefficient spectra of monolayer and bilayer graphene exhibited small dependence on temperature in the near-infrared and visible frequency range. By contrast, the α value in deep UV range progressively increased with increasing temperature. We estimated that the total spectral weight would be constant at higher photon energies. Additional temperature-dependent optical measurements above 7 eV should be performed to confirm this assumption; however, we performed measurements only up to 6.42 eV. Third, the optical absorption coefficient spectra of monolayer and bilayer graphene can be well fitted by two BWF components. The BWF formula is given by [7,53,54]

$$\alpha(\omega) = \alpha_0 \frac{(1+\varepsilon(\omega)/q_{BWF})2}{1+\varepsilon^2(\omega)}, \quad (2)$$

where $\varepsilon(\omega) = (\omega-\omega_0)/\gamma$, ω_0 is the resonant energy, γ is the effective linewidth, α_0 is α at $\varepsilon(\omega) = 0$, and $1/q_{BWF}$ is the asymmetric factor of the BWF formula. The BWF formula describes the interference effect between the discrete spectra and continuum spectra of optical transitions [55]. When $1/q_{BWF} = 0$, Eq. (2) yields a Lorentzian function, which indicates the absence of interference. Constructive or destructive interference occurs above or below ω_0 depending on the sign of $1/q_{BWF}$ and yields an asymmetrical line shape around ω_0. The two BWF fitted curves to α are presented for monolayer and bilayer graphene in Fig. 3 (c) and 3(d) and the fitted parameters are listed in Table 2. In Supplementary Fig. 4, we compared the spectral weight ratio of the 2nd BWF to the 1st BWF component in monolayer and bilayer graphene with that of single-crystal graphite at 300 K. It follows the single-exponential decay trend. Monolayer graphene exhibited a distinct 2nd BWF component compared to bilayer graphene and single-crystal graphite.

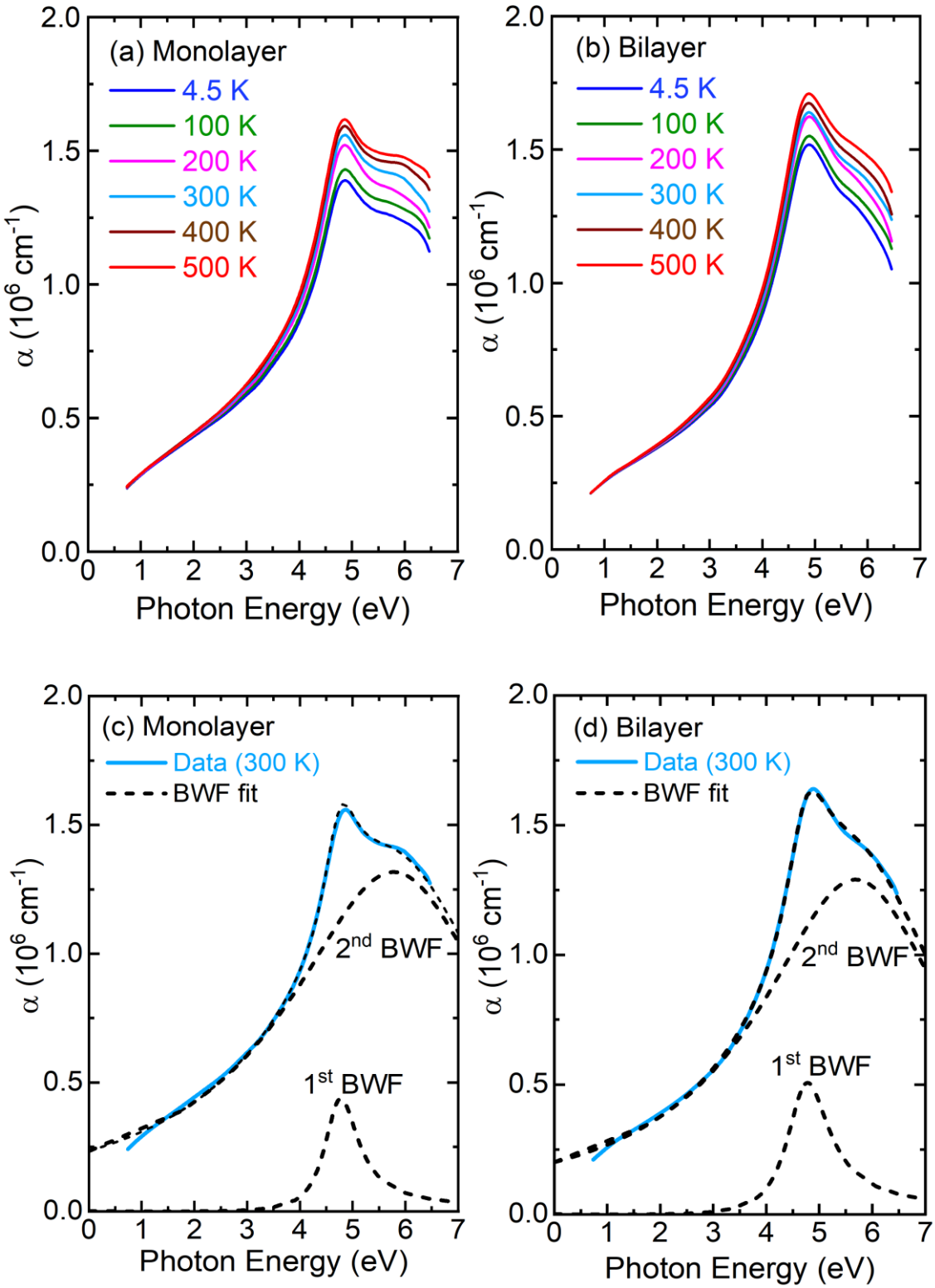

Fig. 3. Temperature-dependent optical absorption coefficient spectra of (a) monolayer and (b) bilayer graphene. The (c) and (d) illustrate the fitting results of spectra obtained at 300 K by using the BWF model.

Table 2. Fitted parameters of BWF to the optical absorption coefficient spectra of monolayer and bilayer graphene at room temperature.

Peak	Parameter	Monolayer	Bilayer
1st BWF	ω_1 (eV)	4.728 ± 0.005	4.712 ± 0.002
	γ_1 (eV)	0.38 ± 0.01	0.48 ± 0.01
	α_0 (cm^{-1})	(0.43 × 10^6) ± 0.01	(0.49 × 10^6) ± 0.01
	$1/q_{BWF}$	0.12 ± 0.01	0.13 ± 0.01
2nd BWF	ω_2 (eV)	5.87 ± 0.01	5.76 ± 0.01
	γ_2 (eV)	2.44 ± 0.01	2.22 ± 0.01
	α_0 (cm^{-1})	(1.31 × 10^6) ± 0.02	(1.28 × 10^6) ± 0.01
	$1/q_{BWF}$	-0.04 ± 0.01	-0.03 ± 0.01

In Fig. 4 (a) and 4(b), we plot the peak energy ω_0, linewidth γ, peak intensity α_0, and asymmetric factor $1/q_{BWF}$ as a function of temperature for the first and second BWF functions for monolayer and bilayer graphene, respectively. The dependence of all the parameters on temperature was similar between monolayer and bilayer graphene, except for $1/q_{BWF}$. With an increase in temperature, ω_0 decreased, γ decreased, and α_0 increased. This temperature-dependent trend was stronger for monolayer and bilayer graphene than for single-crystal graphite [7]. Notably, the $1/q_{BWF}$ values of two optical absorptions were positive and negative, respectively, indicating the difference in their intrinsic nature. The absolute values of two $1/q_{BWF}$ of two BWF components decreased with increasing temperature, reflecting a decrease in the effect of interference $\omega_0(T)$ and $\gamma(T)$ were fitted by the Bose–Einstein model [56] as follows:

$$\omega_0(T) = a - b\left[1 + \frac{2}{e^{\frac{\Theta}{T}} - 1}\right], \tag{3}$$

and

$$\gamma(T) = \Gamma_o\left[1 + \frac{2}{e^{\frac{\Theta}{T}} - 1}\right] + \Gamma_1, \tag{4}$$

where a and Γ_1 represent ω_0 and γ at T = 0 K, respectively; b and Γ_o are associated with the strength of electron–phonon interactions, and Θ is the averaged phonon temperature. The solid lines in Fig. 4(a) and 4(b) represent the fitting using Eqs. (3) and (4). The fitted values are summarized in Table 3. The b and Γ_o values were positive and negative, respectively, for both monolayer and bilayer graphene. The positive value of b indicated that the peak shifted to lower energy with an increase in temperature. The negative value

of Γ_o reflected the long lifetime of electronic states for monolayer and bilayer graphene when temperature increased from 4.5 to 500 K.

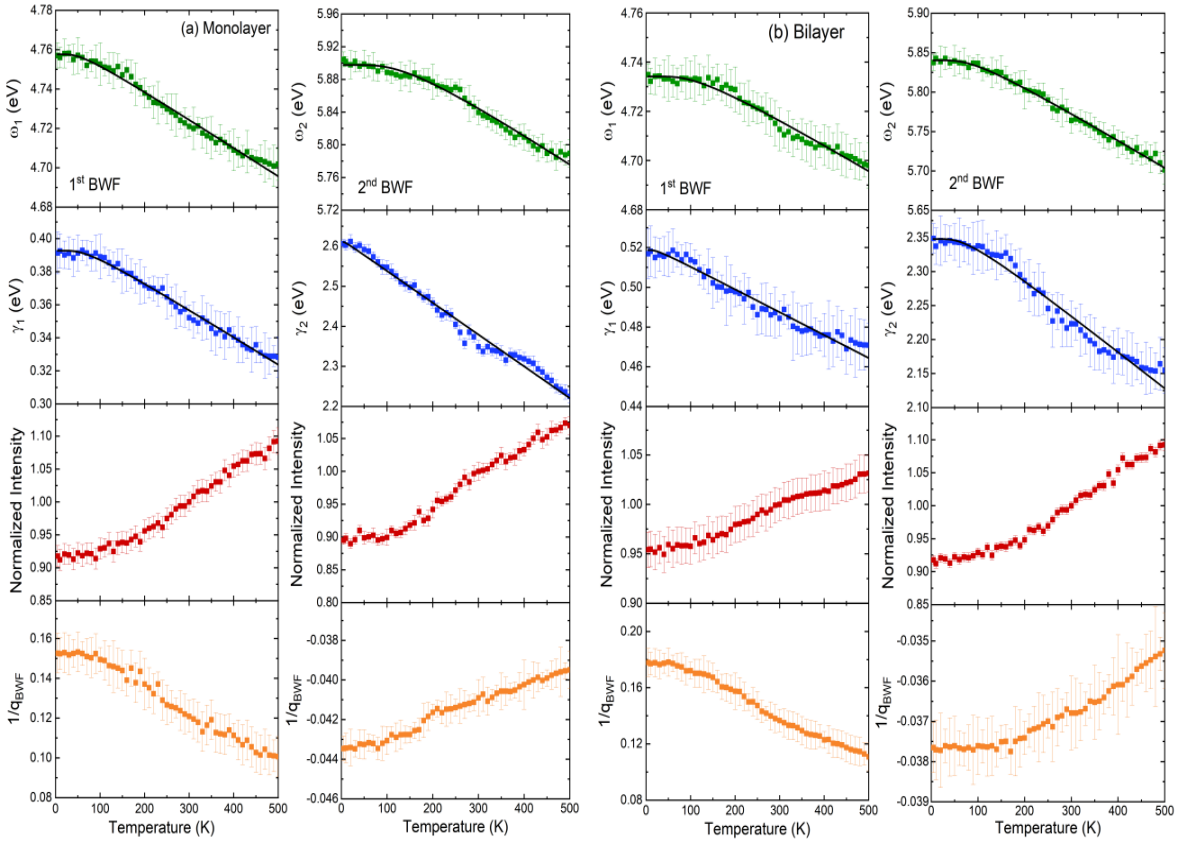

Fig. 4. Temperature-dependent peak energy ω_0, linewidth γ, normalized intensity α_0, and asymmetric factor $1/q_{\mathrm{BWF}}$ of the first and second BWF components in (a) monolayer and (b) bilayer graphene.

Table 3. Fitted parameters of temperature-dependent peak energy $\omega_0(T)$ and linewidth $\gamma(T)$ given by Eqs. (3) and (4) for two BWF components of monolayer and bilayer graphene.

Graphene	Peak	a (eV)	b (meV)	Γ_o (meV)	Γ_1 (eV)	Θ (K)
Monolayer	1st BWF	4.77 ± 0.01	14 ± 2	–15 ± 2	0.408 ± 0.002	379 ± 27
	2nd BWF	5.97 ± 0.01	75 ± 10	–70 ± 14	2.61 ± 0.05	403 ± 38
Bilayer	1st BWF	4.75 ± 0.02	17 ± 3	–32 ± 3	0.522 ± 0.001	324 ± 42
	2nd BWF	5.88 ± 0.01	44 ± 4	–55 ± 13	2.40 ± 0.01	450 ± 29

The implications of optical data are discussed using the first-principles calculations. The observed two optical absorption spectra result from the combination of an excitonic transition at the saddle point (M) in band structures, which is shown by the arrows at the M point in Fig. 5(a) and 5(b), and the collective excitation of surface plasmons [6,7]. The interference of the two optical absorption spectra is expressed by the BWF asymmetric line shape, revealing single-particle electronic excitation coupled to the electronic continuum of plasmonic excitation. With an increase in temperature, the lifetime of surface plasmons decreases through Landau damping, in which a plasmon provides energy to an electron or a hole. Thus, the quantum interference effect between an exciton and a plasmon decreases, leading to (1) a decrease in the BWF asymmetric factor $1/q_{BWF}$, (2) a decrease in the spectral width γ of BWF, and (3) an increase in the peak intensity with an increase in temperature. The continuous spectra of surface plasmons become broad because of the decrease in the lifetime of the plasmon with an increase in temperature, resulting in smaller coupling with discrete single-particle excitation. This leads to an increase in the peak intensity. The observed temperature-dependent interference of excitonic and plasmonic excitations in monolayer and bilayer graphene was considerably larger than that in single-crystal graphite [7]. This finding can be explained by the strong dielectric and quantum confinement effects of electrons on the surface plasmon in 2D materials [6].

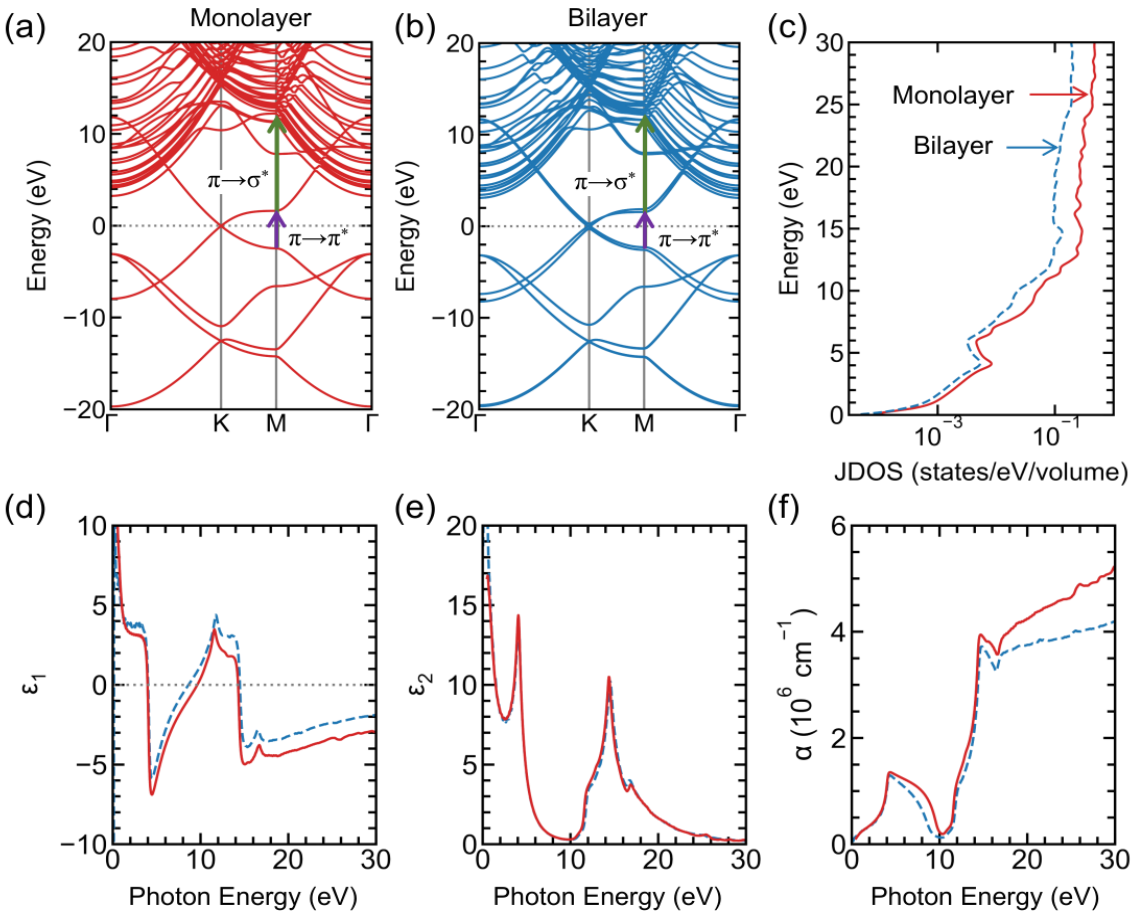

Fig. 5. Energy band structures of (a) monolayer and (b) bilayer graphene. The π → π* and π → σ* interband transitions at saddle M point are denoted by purple and green arrows, respectively. (c) Log plot of the joint density of state (JDOS) of monolayer (solid line) and bilayer (dashed line) graphene. Calculated optical properties including (d) the real part ε_1, (e) imaginary part ε_2, and optical absorption coefficient α as a function of photon energy for monolayer (solid line) and bilayer (dashed line) graphene.

In Fig. 5(a) and 5(b), we plot the electronic energy dispersion of monolayer and bilayer graphene, respectively. The saddle point π → π* and π → σ* transitions at the high-symmetry M point of the Brillouin zone of monolayer or bilayer graphene leads to van Hove-like singularities of the JDOS at around 4.14 (4.17) eV and 14.77 (14.69) eV for monolayer (bilayer) graphene, respectively, as presented in Fig. 5(c). The JDOS is defined as [62]

$$\mathrm{JDOS}(E) = \frac{1}{4\pi^2}\int \mathrm{d}^3k[E_v(k) - E_c(k) - E], \qquad (5)$$

where integration on the wavevector *k* is considered over the hexagonal 2D Brillouin zone, and $E_v(k)$ and $E_c(k)$ are the energies of the valence and conduction bands at *k*, respectively. The JDOS is enhanced when transitions from the flat valence band to the flat conduction band occur, as indicated by arrows in Fig. 5(a) and 5(b). The calculated JDOS peak at 4.1 eV, which corresponds to the $\pi \rightarrow \pi^*$ interband transition, was smaller than the experimental value of around 4.7 eV (see Fig. 3). The energy difference can be explained by the effect of the electron–electron (e–e) self-energy and the electron–hole (e–h) interaction at the M point. By considering only the e–e self-energy within the GW method, Trevisanutto *et al.* [63] reported that the $\pi \rightarrow \pi^*$ transition at the M point occurs at approximately 5 eV. By contrast, by using GW + BSE, which considers both e–e self-energy and e–h interaction, Yang *et al.* [64] indicated that the $\pi \rightarrow \pi^*$ transition occurs at 4.5 eV, which is similar to that observed in this study. In the GW calculation [63], the $\pi \rightarrow \sigma^*$ transition at the M point occurs at 15 eV, which is similar to the present IPA calculation for the $\pi \rightarrow \sigma^*$ transition. Thus, the e–e self-energy effect might not be essential for the $\pi \rightarrow \sigma^*$ transition.

In Fig. 5(d) and 5(e), we present the real part ε_1 and imaginary part ε_2 of the dielectric function for monolayer (solid line) and bilayer (dashed line) graphene. Because the condition to obtain the peak of the optical absorption coefficient α is $\varepsilon_1 = 0$ and $\varepsilon_2 \gg 1$ (see Eq. (1)), two peaks of α are noted at 4.1 eV and 15 eV, as depicted in Fig. 5(f). The calculated α value at 4 eV is approximately 1.4×10^6 cm^{-1} for both monolayer and bilayer graphene, which is consistent with the experimental value of approximately 1.5×10^6 cm^{-1} (Fig. 3). The calculated α value for photon energy ranging from 0 to 7 eV agrees with the finding that the peak of monolayer graphene at 4 eV is more asymmetric than that of bilayer graphene (see the asymmetric factor $1/q_{BWF}$ in Table 2). By considering photon energy up to 30 eV, we determined a second peak of α at 15 eV. The asymmetric behavior of the second peak might be due to the contribution of the $\pi \rightarrow \sigma^*$ plasmon [63]. Determining the high value of photon energy, such as from 10 to 30 eV, experimentally is difficult. Thus, the theoretical calculations can explain not only the $\pi \rightarrow \pi^*$ transition but also the $\pi \rightarrow \sigma^*$ transition at high photon energy.

In Supplementary Fig. 5, we show the calculated electron energy loss spectroscopy (EELS) ($\mathrm{Im}(1/\varepsilon)$) as a function of photon energy for monolayer and bilayer graphene. A

peak consistent with the observed EELS by experiments for monolayer graphene [65], bilayer graphene [66], and graphite [67] is found around 5-6 eV as π plasmon. Since α is proportional to ε_2, the peak position of α should coincide with the local maximum of ε_2. In Fig. 5(e), we found only one local maximum of ε_2 at 4.1 eV. On the other hand, in Fig. 3, α shows two peaks corresponding to two fitting BWF lines. These findings suggest that the first peak around 4.7 eV is related to the local maximum of ε_2, resulting from interband $\pi \rightarrow \pi^*$ transitions, while the second peak around 5.8 eV is associated with the interband surface plasmon. In undoped graphene, both single particle excitation and interband collective excitation can occur simultaneously, leading to an interference effect.

4. Summary

We combined spectroscopic ellipsometry and first-principles calculations to investigate the fundamental optical excitation of monolayer and bilayer graphene. The optical absorption spectra of monolayer and bilayer graphene at room temperature are expressed by two BWF components in the deep UV frequency region, indicating an interference effect between discrete spectra and continuous spectra. We assigned the observed BWF resonances to an excitonic transition at the saddle point (M) in band structures and collective excitation of the surface plasmons. These two BWF absorption spectra exhibited a redshift and narrowed under an increased intensity at elevated temperatures. This unusual temperature-dependent behavior can be attributed to a decreased quantum interference effect between the exciton and surface plasmons because of the damping of surface plasmons at the higher temperature. Our results not only provide microscopic insights into the quasiparticle band structures and collective excitations of graphene but also highlight the unique characteristics and potential of graphene for use in deep UV optoelectronic and photonic device applications.

ACKNOWLEDGEMENTS

H.L.L. thanks the Ministry of Science and Technology of Republic of China for its financial support under Grant No. MOST 111-2112-M-003-016. R.S. acknowledges JSPS

KAKENHI (Nos. JP18H01810, JP22H00283). H.A. acknowledges JSPS KAKENHI (No. JP21H05232, JP21H05233, 21K18878) and JST-CREST (No. JPMJCR18I1, JPMJCR20B1). N.T.H. acknowledges JSPS KAKENHI (No. JP20K15178).

AUTHOR CONTRIBUTIONS

H. L. L. conceived the research and was responsible for the experimental design. B.D.A. and D.P.G. conducted the experiments. P.S.F., K.K., and H.A. were responsible for the sample preparation. N.T.H. and R.S. performed the first-principles calculations and theoretical analyses. H.L.L., B.D.A, P.S.F, N.T.H, and R.S. drafted the paper. All contributing authors have discussed the results and provided their comments regarding the manuscript.

DATA AVAILABILITY STATEMENT

The data that support the findings of this study are available from the corresponding author upon reasonable request.

ADDITIONAL INFORMATION

The authors declare no competing interests.

REFERENCES

1. A. N. Grigorenko, M. Polini, and K. S. Novoselov, Graphene plasmonics, Nature Photonics **6**, 749 (2012).
2. J. Chen, M. Badioli, P. A.-Gonzalez, S. Thongrattanasiri, F. Huth, J. Osmond, M. Spasenovic, A. Centeno, A. Pesquera, P. Godignon, A. Z. Elorza, N. Camara, F. J. G. de Abajo, R. Hillenbrand, and F. H. L. Koppens, Optical nano-imaging of gate-tunable graphene plasmons, Nature **487**, 77 (2012).
3. Z. Fei, A. S. Rodin, G. O. Andreev, W. Bao, A. S. McLeod, M. Wagner, L. M. Zhang, Z. Zhao, M. Thiemens, G. Dominguez, M. M. Fogler, A. H. Castro Neto, C. N. Lau, F. Keilmann, and D. N. Basov, Gate-tuning of graphene plasmons revealed by infrared

nano-imaging, Nature **487**, 82 (2012).

4. Y. Li, Z. Li, C. Chi, H. Shan, L. Zheng, and Z. Fang, Plasmonics for 2D nanomaterials: properties and applications, Advance Science **4**, 1600430 (2017).

5. C. Song, X. Yuan, C. Huang, S. Huang, Q. Xing, C. Wang, C. Zhang, Y. Xie, Y. Lei, F. Wang, L. Mu, J. Zhang, F. Xiu, and H. Yan, Plasmons in the van der Waals charge-density-wave material 2H-$TaSe_2$, Nature Communication **12**, 386 (2021).

6. M. S. Ukhtary and R. Saito, Surface plasmons in graphene and carbon nanotubes, Carbon **167**, 455 (2020).

7. D. P. Gulo, N. T. Hung, T. J. Yang, G. J. Shu, R. Saito, and H. L. Liu, Exploring unusual temperature-dependent optical properties of graphite single crystals by spectroscopic ellipsometry, Carbon **197**, 485 (2022).

8. K. S. Novoselov, A. K. Geim, S. V. Morozov, D. Jiang, Y. Zhang, S. V. Dubonos, I. V. Grigorieva, and A. A. Firsov, Electric field effect in atomically thin carbon films, Science **306**, 666 (2004).

9. A. K. Geim and K. S. Novoselov, The rise of graphene, Nature Materials **6**, 183 (2007).

10. A. K. Geim, Graphene: status and prospects, Science **324**, 1530 (2009).

11. A. H. Castro Neto, F. Guinea, N. M. R. Peres, K. S. Novoselov, and A. K. Geim, The electronic properties of graphene, Rev. Mod. Phys. **81**, 109 (2009).

12. V. N. Kotov, B. Uchoa, V. M. Pereira, F. Guinea, and A. H. Castro Neto, Electron–electron interactions in graphene: current status and perspectives. Rev. Mod. Phys. **84**, 1067 (2012).

13. C. R. Woods, L. Britnell, A. Eckmann, R. S. Ma, J. C. Lu, H. M. Guo, X. Lin, G. L. Yu, Y. Cao, R. V. Gorbachev, A. V. Kretinin, J. Park, L. A. Ponomarenko, M. I. Katsnelson, Yu. N. Gornostyrev, K. Watanabe, T. Taniguchi, C. Casiraghi, H.-J. Gao, A. K. Geim, and K. S. Novoselov, Commensurate-incommensurate transition in graphene on hexagonal boron nitride, Nature Physics **10**, 451 (2014).

14. X. Wang, L. Zhi, and K. Mullen, Transparent, conductive graphene electrodes for dye-sensitized solar cells, Nano Lett. **8**, 323 (2008).

15. P. Blake, P. D. Brimicombe, R. R. Nair, T. J. Booth, D. Jiang, F. Schedin, L. A. Ponomarenko, S. V. Morozov, H. F. Gleeson, E. W. Hill, A. K. Geim, and K. S. Novoselov, Graphene-based liquid crystal device, Nano Lett. **8**, 1704 (2008).

16. F. Xia, T. Mueller, Y.-M. Lin, A. Valdes-Garcia, and P. Avouris, Ultrafast graphene photodetector, Nature Nanotechnology **4**, 839 (2009).

17. T. Mueller, F. Xia, and P. Avouris, Graphene photodetectors for high-speed optical communications, Nature Photonics **4**, 297 (2010).

18. P. Avouris and C. Dimitrakopoulos, Graphene: synthesis and applications, Materials Today **15**, 86 (2012).

19. G.H. Li, A. Luican, J.M.B. Lopes dos Santos, A.H. Castro Neto, A. Reina, J. Kong, and

E.Y. Andrei, Observation of Van Hove singularities in twisted graphene layer, Nature Physics **6**, 109 (2010).

20. Y. Jiang, J. Mao, X. Lai, K. Watanabe, T. Taniguchi, K. Haule, and E.Y. Andrei, Charge-order and broken rotational symmetry in magic angle twisted bilayer graphene, Nature **573**, 91 (2019).

21. A. Jaoui, I. Das, G. Di Battista, J. Díez-Mérida, X. Lu, K. Watanabe, T. Taniguchi, H. Ishizuka, L. Levitov, and D. K. Efetov, Quantum critical behaviour in magic-angle twisted bilayer graphene, Nature Physics **18**, 633 (2022).

22. A. M. Seiler, F. R. Geisenhof, F. Winterer, K. Watanabe, T. Taniguchi, T. Xu, F. Zhang, and R. T. Weitz, Quantum cascade of correlated phases in trigonally warped bilayer graphene, Nature **608**, 298 (2022).

23. F. K. de Vries, E. Portoles, G. Zheng, T. Taniguchi, K. Watanabe, T. Ihn, K. Ensslin, and P. Rickhaus, Gate-defined Josephson junctions in magic-angle twisted bilayer graphene, Nature Nanotechnology **16**, 760 (2021).

24. D. Rodan-Legrain, Y. Cao, J. M. Park, S. C. de la Barrera, M. T. Randeria, K. Watanabe, T. Taniguchi, and P. Jarillo-Herrero, Highly tunable junctions and non-local Josephson effect in magic-angle graphene tunneling devices, Nature Nanotechnology **16**, 769 (2021).

25. F. Wang, Y. Zhang, C. Tian, C. Girit, A. Zettl, M. Crommie, and Y. R. Shen, Gate-variable optical transitions in graphene, Science **320**, 206 (2008).

26. Z. Q. Li, E. A. Henriksen, Z. Jiang, Z. Hao, M. C. Martin, P. Kim, H. L. Stormer, and D. N. Basov, Dirac charge dynamics in graphene by infrared spectroscopy, Nature Physics **4**, 532 (2008).

27. K. F. Mak, M. Y. Sfeir, Y. Wu, C. H. Lui, J. A. Misewich, and T. F. Heinz, Measurement of the optical conductivity of graphene, Phys. Rev. Lett. **101**, 196405 (2008).

28. L. Ren, Q. Zhang, J. Yao, Z. Sun, R. Kaneko, Z. Yan, S. Nanot, Z. Jin, I. Kawayama, M. Tonouchi, J. M. Tour, and J. Kono, Terahertz and infrared spectroscopy of gated large-area graphene, Nano Lett. **12**, 3771 (2012).

29. X. Zou, J. Shang, J. Leaw, Z. Luo, L. Luo, C. La-o-vorakiat, L. Cheng, S. A. Cheong, H. Su, J. X. Zhu, Y. Liu, K. P. Loh, A. H. Castro Neto, T. Yu, and E. E. M. Chia, Terahertz conductivity of twisted bilayer graphene, Phys. Rev. Lett. **110**, 067401 (2013).

30. L. Yang, J. Deslippe, C. H. Park, M. L. Cohen, and S. G. Louis, Excitonic effects on the optical response of graphene and bilayer graphene, Phys. Rev. Lett. **103**, 186802 (2009).

31. V. G. Kravets, A. N. Grigorenko, R. R. Nair, P. Blake, S. Anissimova, K. S. Novoselov, and A. K. Geim, Spectroscopic ellipsometry of graphene and an exciton-shifted van Hove peak in absorption, Phys. Rev. B **81**, 155413 (2010).

32. U. Wurstbauer, C. Roling, U. Wurstbauer, W. Wegscheider, M. Vaupel, P. H. Thiesen, and D. Weiss, Imaging ellipsometry of graphene, Appl. Phys. Lett. **97**, 231901 (2010).

33. D. H. Chae, T. Utikal, S. Weisenburger, H. Giessen, K. v. Klitzing, M. Lippitz, and J.

Smet, Excitonic Fano resonance in free-standing graphene, Nano Lett. **11**, 1379 (2011).

34. I. Santoso, P. K. Gogoi, H. B. Su, H. Huang, Y. Lu, D. Qi, W. Chen, M. A. Majidi, Y. P. Feng, A. T. S. Wee, K. P. Loh, T. Venkatesan, R. P. Saichu, A. Goos, A. Kotlov, M. Rubhausen, and A. Rusydi, Observation of room-temperature high-energy resonant excitonic effects in graphene, Phys. Rev. B **84**, 081493 (2011).

35. W. Li, G. Cheng, Y. Liang, B. Tian, X. Liang, L. Peng, A. R. H. Walker, D. J. Gundlach, and N. V. Nguyen, Broadband optical properties of graphene by spectroscopic ellipsometry, Carbon **99**, 348 (2016).

36. M. Fang, H. Gu, B. Song, Z. Guo, and S. Liu, Thickness and layer stacking order effects on complex optical conductivity and exciton strength of few-layer graphene: implications for optical modulators and photodetectors, ACS Appl. Nano Mater. **5**, 1864 (2022).

37. M. A. El-Sayed, G. A. Ermolaev, K. V. Voronin, R. I. Romanov, G. I. Tselikov, D. I. Yakubovsky, N. V. Doroshina, A. B. Nemtsov, V. R. Solovey, A. A. Voronov, S. M. Novikov, A. A. Vyshnevyy, A. M. Markeev, A. V. Arsenin, and V. S. Volkov, Optical constants of chemical vapor deposited graphene for photonic applications, Nanomaterials **11**, 1230 (2021).

38. S. Wu, L. Wan, L. Wei, D. N. Talwar, K. He, and Z. Feng, Temperature-dependent optical properties of graphene on Si and SiO_2/Si substrates, Crystals **11**, 358 (2021).

39. T. Igarashi, H. Kawai, K. Yanagi, N. T. Cuong, S. Okada, and T. Pichler, Tuning localized transverse surface plasmon resonance in electricity-selected single-wall carbon nanotubes by electrochemical doping, Phys. Rev. Lett. **114**, 176807 (2015).

40. K. Yanagi, R. Okada, Y. Ichinose, Y. Yomogida, F. Katsutani, W. Gao, and J. Kono, Intersubband plasmons in the quantum limit in gated and aligned carbon nanotubes, Nature Communication **9**, 1121 (2018).

41. D. Satco, D. S. Kopylova, F. S. Fedorov, T. Kallio, R. Saito, and A. G. Nasibulin, Intersubband plasmon observation in electrochemically gated carbon nanotube films, ACS Appl. Electron. Mater. **2**, 195 (2020).

42. K. I. Sasaki, S. Murakami, and H. Yamamoto, Theory of intraband plasmons in doped carbon nanotubes: rolled surface-plasmons of graphene, Appl. Phys. Lett. **108**, 163109 (2016).

43. D. Satco, A. R. T. Nugraha, M. S. Ukhtary, D. Kopylova, A. G. Nasibulin, and R. Saito, Intersubbad plasmon excitations in doped carbon nanotubes, Phys. Rev. B **99**, 075403 (2019).

44. Y. Ogawa, B. Hu, C.M. Orofeo, M. Tsuji, K. Ikeda, S. Mizuno, H. Hibino, and H. Ago, Domain structure and boundary in single-layer graphene grown on Cu(111) and Cu(100) films, J. Phys. Chem. Lett. **3**, 219 (2012).

45. H. Ago, K. Kawahara, Y. Ogawa, S. Tanoue, M.A. Bissett, M. Tsuji, H. Sakaguchi, R.J. Koch, F. Fromm, T. Seyller, K. Komatsu, and K. Tsukagoshi, Epitaxial growth and electronic properties of large hexagonal graphene domains on Cu(111) thin film, Appl. Phys. Express **6**, 075101 (2013).

46. B. Hu, H. Ago, Y. Ito, K. Kawahara, M. Tsuji, E. Magome, K. Sumitani, N. Mizuta, K. Ikeda, and S. Mizuno, Epitaxial growth of large-area single-layer graphene over Cu(111)/sapphire by atmospheric pressure CVD, Carbon **50**, 57 (2012).

47. P. Solis-Fernández, Y. Terao, K. Kawahara, W. Nishiyama, T. Uwanno, Y. C. Lin, K. Yamamoto, H. Nakashima, K. Nagashio, H. Hibino, K. Suenaga, and H. Ago, Isothermal growth and stacking evolution in highly uniform Bernal-stacked bilayer graphene, ACS Nano **14**, 6844 (2020).

48. H. L. Liu, T. Yang, J. H. Chen, H. W. Chen, H. Guo, R. Saito, M. Y. Li, and L. J. Li, Temperature-dependent optical constants of monolayer MoS_2, $MoSe_2$, WS_2, and WSe_2: spectroscopic ellipsometry and first-principles calculations, Scientific Reports **10**, 15282 (2020).

49. H. W. Chen, C. Y. Huang, G. J. Shu, and H. L. Liu, Temperature-dependent optical properties of $CuFeO_2$ through the structural phase transition, RSC Adv. **11**, 40173 (2021).

50. H. Laysandra, Y. C. Chao, and H. L. Liu, Assessing optical properties of $CH_3NH_3PbBr_3$ single crystals across the structural phase transition by spectroscopic ellipsometry, J. Phys. Chem. C **126**, 797 (2022).

51. E. Hecht, Optics (Addison Wesley, San Francisco, 2002).

52. J. A. McCaulley, V. M. Donnelly, M. Vernon, and I. Taha, Temperature dependence of the near-infrared refractive index of silicon, gallium arsenide, and indium phosphide, Phys. Rev. B **49**, 7408 (1994).

53. G. Breit and E. Wigner, Capture of slow neutrons, Phys. Rev. **49**, 519 (1936).

54. E. H. Hasdeo, A. R. T. Nugraha, M. S. Dresselhaus, and R. Saito, Breit-Wigner-Fano line shapes in Raman spectra of graphene, Phys. Rev. B **90**, 245140 (2014).

55. J. F. Scott, Soft-mode spectroscopy: Experimental studies of structural phase transitions, Rev. Mod. Phys. **46**, 83 (1974).

56. L. Vina, S. Logothetidis, and M. Cardona, Temperature dependence of the dielectric function of germanium, Phys. Rev. B **30**, 1979 (1984).

57. P. Giannozzi, S. Baroni, N. Bonini, M. Calandra, R. Car, C. Cavazzoni, D. Ceresoli, G.L. Chiarotti, M. Cococcioni, I. Dabo, et al., Quantum ESPRESSO: a modular and open-source software project for quantum simulations of materials, J. Phys. Condens. Matter **21**, 395502 (2009).

58. J.P. Perdew, A. Zunger, Self-interaction correction to density-functional approximations for many-electron systems, Phys. Rev. B **23,** 5048 (1981).

59. C. Hartwigsen, S. Goedecker, and J. Hutter, Relativistic separable dual-space Gaussian pseudopotentials from H to Rn, Phys. Rev. B **58**, 3641 (1998).

60. R. Sabatini, T. Gorni, S. Gironcoli, Nonlocal van der Waals density functional made simple and efficient, Phys. Rev. B **87** (2013), 041108(R).

61. T. Ohta, A. Bostwick, T. Seyller, K. Horn, and E. Rotenberg, Controlling the electronic structure of bilayer graphene, Science **313**, 951-954 (2006).

62. V. V. Thanh, N. D. Van, D. V. Truong, R. Saito, and N. T. Hung, First-principles study of mechanical, electronic and optical properties of Janus structure in transition metal dichalcogenides, Appl. Surf. Sci. **526,** 146730 (2020).

63. P. E. Trevisanutto, C. Giorgetti, L. Reining, M. Ladisa, and V. Olevano, Ab initio GW many-body effects in graphene, Phys. Rev. Lett. **101**, 226405 (2008).

64. L. Yang, J. Deslippe, C. H. Park, M. L. Cohen, and S. G. Louie, Excitonic effects on the optical response of graphene and bilayer graphene, Phys. Rev. Lett. **103**, 186802 (2009).

65. M. H. Gass, U. Bangert, A. L. Bleloch, P. Wang, R. R. Nair and A. K. Geim, Free-standing graphene at atomic resolution, Nat. Nanotechnol. **3**, 676 (2008).

66. T. Eberlein, U. Bangert, R. R. Nair, R. Jones, M. Gass, A. L. Bleloch, K. S. Novoselov, A. Geim, and P. R. Briddon, Plasmon spectroscopy of free-standing graphene films, Phys. Rev. B **77**, 233406 (2008).

67. M. Filippi and L. Calliari, Measuring the energy of the graphite $\pi + \sigma$ plasmon peak, Surf. Interface Anal. **38**, 595 (2006).